





On the Ability of PolSAR Measurements to Discriminate Among Mangrove Species

Emanuele Ferrentino , *Student Member, IEEE*, Ferdinando Nunziata , *Senior Member, IEEE*, Hongsheng Zhang , *Member, IEEE*, and Maurizio Migliaccio , *Fellow, IEEE*

Abstract—In this article, a polarimetric synthetic aperture radar (PolSAR) feature is analyzed to discriminate among different mangrove species. This feature, which is related to the Wishart distance, maximizes the contrast among mangrove species optimizing the ratio between quadratic forms. The discrimination performance is assessed both against ground truth and by intercomparing it with conventional model-based decomposition features. Results obtained by processing actual *L*- and *C*-band full-polarimetric synthetic aperture radar scenes collected by ALOS-PALSAR-2 and RADARSAT-2 missions show that the proposed approach achieves accurate enough discrimination performance to differentiate two out of the four mangrove species. In addition, results suggest using a multifrequency PolSAR approach to maximize discrimination performance.

Index Terms—Change detection, classification, mangroves, polarimetric synthetic aperture radar (PolSAR).

I. INTRODUCTION

MANGROVE forests are coastal wetlands that contribute to biodiversity and act as a major biogeochemical link between upland and coastal regions. For this reason, they play a major role in the coastal ecosystem and sea coast conservation. In fact, they provide a useful buffer that separates land from sea. They are a sink for sediment and nutrient run-off, and they form a barrier protecting the land from marine inundation during storms. However, mangrove forests are a very critical ecosystem that is severely threatened especially by human activities. It has been estimated that about 50% of the global mangrove area has disappeared since 1900 with the strongest reduction occurred in the past two decades [1]. The dominant factor responsible for this reduction is the conversion of mangroves to other land areas. In addition, mangrove forests are also very sensitive to climate change with the main driver of mangrove problems being the sea level rise. All this matter suggests developing a monitoring system that should assess mangrove extent, community structure, status, and health [1].

Manuscript received August 2, 2019; revised December 2, 2019 and January 31, 2020; accepted April 20, 2020. Date of publication May 28, 2020; date of current version June 11, 2020. (Corresponding author: Maurizio Migliaccio.)

Emanuele Ferrentino, Ferdinando Nunziata, and Maurizio Migliaccio are with the Dipartimento di Ingegneria, Università degli Studi di Napoli “Parthenope”, 80133 Napoli, Italy (e-mail: emanuele.ferrentino@uniparthenope.it; ferdinando.nunziata@uniparthenope.it; mnm.migliaccio@gmail.com).

Hongsheng Zhang is with the Department of Geography, The University of Hong Kong, Pok Fu Lam, Hong Kong (e-mail: zhanghs@hku.hk).

Digital Object Identifier 10.1109/JSTARS.2020.2989872

Within this context, observing mangroves from space using remote sensing tools offers unprecedented advantages. In fact, despite the importance of mangrove forests, reliable, accurate, and timely information on mangrove types, extent, etc., is very often not available. Attempts to build datasets of world-wide mangrove-covered areas are provided in [2], where a globally consistent and repeatable methodology is described to produce a high-resolution mangrove dataset using Global Land Survey and Landsat data. The main source of remotely sensed information about mangrove forests comes from optical sensors. In fact, mangroves possess a well-recognizable signature in the visible spectral range of red and the near and mid infrared [3]. In [4], first attempts to use remotely sensed data collected by the microwave synthetic aperture radar (SAR) with the aim of globally observing mangroves are provided using *L*-band SAR collected by the Japanese ALOS PALSAR mission. The classification strategy is based on HH and HV channels that are processed using the extremely randomized trees classifier. In [5] and [6], unsupervised classifiers and machine learning methods are proposed to deal with multisensor data (mainly optical and SAR) for mangrove observation. Although there is a broad literature focused on the observation of mangrove extent, the discrimination of different mangrove species plays a key role in the analysis of mangrove forests [7]. This task is typically addressed using high-to-very-high spatial resolution remotely sensed data mainly coming from optical satellites that are processed using object-based image analysis tools and exploiting time series [8]–[12]. There are only few studies, e.g., [13], where SAR and optical data are jointly used to deal with the discrimination of mangrove species. Experimental results obtained using optical WorldVIEW and dual-polarimetric (DP) RadarSAT-2 SAR data show a good capability to discriminate different mangrove species. In [14], mangrove forests are mapped using frequency-based contextual classification. Experimental results, undertaken processing *L*-band ALOS/PALSAR images, show that the mangrove forests are well detected with some misclassification occurring between mangroves and urban areas. In [15], a time series of optical Landsat-7/8 and SAR Sentinel-1 imagery is exploited to map the mangrove forest in the southern China. The integration of the Sentinel-1A VH channel and the modified normalized difference water index shows great potential in identifying yearlong tidal and fresh water bodies. In [16], a suite of methods to combine Landsat-8, ALOS PALSAR, and SRTM data is used for mapping spatial distribution of mangrove composition. Results show that

the combination of multispectral and SAR data provides very accurate mangroves maps.

To the best of authors' knowledge, there are few studies that explicitly addressed the discrimination of mangrove species using multipolarization SAR measurements. In [17], mangrove species are mapped using the logistic model tree classifier. Experimental results, undertaken processing ALOS-2 imagery, show that two mangrove species (*Kandelia obovata* (KO) and *Sonneratia caseolaris*) are mainly discriminated. In [18], model-based and eigen-based decompositions are applied to *L*-band ALOS PALSAR imagery to analyze their sensitivity to mangrove species. Results confirm the added value provided by polarimetric SAR (PolSAR) measurements in catching scattering-based information related to mangroves. No classification is performed because of the lack of pure stands.

In this study, the sensitivity of PolSAR information to different mangrove species is analyzed with the goal of discriminating among mangrove species. A processing chain is proposed that consists of a change detector approach that is based on the optimization of the ratio between quadratic forms [19], [20]. This optimization procedure, also referred as polarimetric matched filter [19], is here studied for the discrimination among mangrove species. In particular, we maximize the contrast among polarimetric signatures related to the mangrove species. Then, to objectively discuss the discrimination capability, a decision tree classifier is applied to partition the output space into a number of classes that correspond to the four mangrove species identified by ground truth information. This study focuses on an important area of interest, namely the Mai Po Marshes Nature Reserve (MPMNR), Hong Kong. Results verified against ground truth samples show that the proposed processing chain can be used to assist conventional optical-based approaches in mapping mangrove species. The main outcomes can be summarized as follows.

- 1) The optimization procedure results in a feature that is related to the well-known Wishart distance [21]–[24].
- 2) The approach discriminates two out of the four mangrove species.
- 3) The proposed feature, together with the decision tree classifier, outperforms at both *L*- and *C*-band conventional model-based features and the Wishart classifier.
- 4) *L*- and *C*-band PolSAR measurements can be jointly used to maximize discrimination performance.

The rest of this article is organized as follows. In Section II, the test site and the dataset are described. The methodological facts are described in Section III, while Section IV presents selected experiments. Section V concludes this article.

II. TEST SITE AND DATASET

The test area includes different mangrove species and is related to the MPMNR, Hong Kong (see Fig. 1). There are around 350 hectares of mangrove forests in the Core Zone of the MPMNR that include KO, *Avicennia marina* (AM), *Acanthus ilicifolius* (AI), *Aegiceras corniculatum* (AC), and *Sonneratia apetala* (see Fig. 2) [13]. The mangrove species are annotated in the Worldview-3 image collected on June 2, 2016, using



Fig. 1. Worldview-3[®] image related to the MPMNR and collected on June 2, 2016. Note that the four mangrove species are also annotated according to the ground truth information.

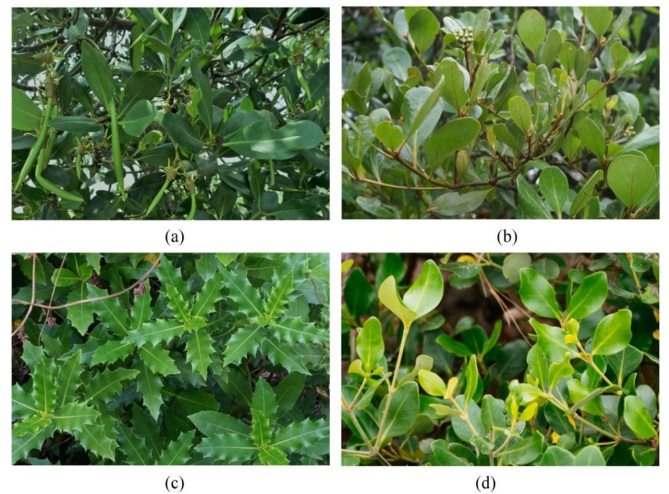


Fig. 2. Pictures related to the mangrove species populating MPMNR, Hong Kong, according to the available ground truth. Adopted from [13]. (a) *Kandelia obovata*. (b) *Avicennia marina*. (c) *Acanthus ilicifolius*. (d) *Aegiceras corniculatum*.

ground information that consists of a set of 718 samples collected using GPS receivers and cameras during two surveys over the MPMNR on July 11, 2013 and November 10 2015 (see Fig. 1).

The satellite dataset consists of two single-look complex full-polarimetric (FP) SAR images collected by the *C*-band RadarSAT-2 and the *L*-band ALOS-2 FP SAR on July 12,

TABLE I
 SAR DATASET ACQUIRED BY RADARSAT-2 AND ALOS-2

Sensor	Acquisition date	Band	Angle of incidence (AoI) (°)	Acquisition mode
RADARSAT-2	12/07/2015	C	35	Ascending
ALOS-2	31/12/2015	L	31	Descending

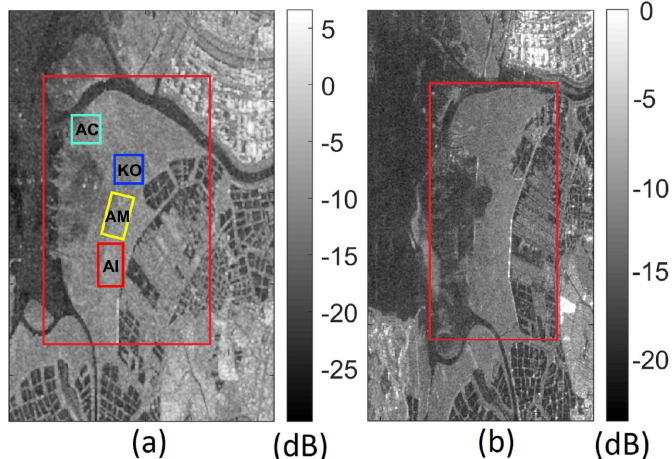


Fig. 3. Excerpts of the VV-polarized SAR scene collected by the (a) C-band RadarSAT-2 and (b) L-band ALOS-2 PALSAR SARs. Note that the red box stands to highlight the area that includes mangrove forests and the four ROIs considered to evaluate the λ statistical distribution. Note that the same ROIs refer also to the ALOS-2 PALSAR image.

2015 and December 31, 2015, respectively (see Table I). The ground-projected excerpts of the RadarSAT-2 and ALOS-2 SAR imagery are shown in Fig. 3(a) and (b), respectively.

III. METHODOLOGY

In this section, theoretical facts that lie at the basis of the approach proposed to discriminate among mangrove species in multipolarization SAR data are described.

A processing chain that consists of three steps is proposed. The first step is to preprocess SAR imagery by applying a 5×5 boxcar speckle filter and geocoding the SAR scenes. The second step consists of implementing a change detection scheme that exploits multipolarization information to maximize the contrast among polarimetric scattering resulting from mangrove species. The third step consists of analyzing in an objective way the discrimination performance of the PolSAR feature resulting from the change detector. Hence, an unsupervised decision tree classifier is applied, and the discrimination performance is discussed against ground truth and conventional PolSAR features derived from model-based decompositions using a confusion matrix.

In the following, the last two steps are fully described.

The change detection approach relies on the PMF, developed by Novak *et al.* [19] to deal with the optimization of the target-to-clutter ratio using a single PolSAR image, that has been extended in [20] to deal with the optimization of the power ratio between two different PolSAR acquisitions. In this study, the key idea is looking for the scattering mechanism $\underline{\omega}_{\max}$ that maximizes the

ratio between the power associated with a reference area with respect to the power of a target area that is evaluated using a sliding window that scans the whole SAR scene, i.e., we aim at maximizing the following target-to-reference power ratio:

$$\rho_{12} = \frac{\underline{\omega}^\dagger \mathbf{C}_{11} \underline{\omega}}{\underline{\omega}^\dagger \mathbf{C}_{22} \underline{\omega}} \quad (1)$$

where \mathbf{C}_{22} and \mathbf{C}_{11} are covariance matrices that describe the reference scenario and the test area, respectively, $\underline{\omega}$ is the projecting vector, and \dagger stands for complex conjugate transpose. Both covariance matrices are estimated using a 5×5 boxcar window. To search for $\underline{\omega}_{\max}$, an optimization problem is to be addressed that can be formulated using the Lagrangian method [20], [25]–[27]. The latter is applied to the quadratic form $\underline{\omega}^\dagger \mathbf{C}_{CD} \underline{\omega}$, where the change matrix \mathbf{C}_{CD} is given by

$$\mathbf{C}_{CD} = \mathbf{C}_{11} \mathbf{C}_{22}^{-1}. \quad (2)$$

Hence, the following eigenvalue problem is obtained [19]:

$$\mathbf{C}_{CD} \underline{\omega} = \lambda_i \underline{\omega} \quad (3)$$

with λ_i being the real and positive eigenvalues that maximize/minimize the change matrix, i.e., they are the eigenvalues that maximize/minimize the contrast between the polarimetric backscattering of the test area with respect to the reference area. Hence, the following feature is considered:

$$\lambda = \frac{1}{N} \sum_{i=1}^N \lambda_i \quad (4)$$

where $N = 2(3)$ when DP (FP) data are available. The proposed approach is not only operationally interesting since it enhances the contrast in terms of polarimetric signatures in a very computer-time effective way, but it can be also adapted to the amount of polarimetric information available. In fact, when the FP SAR is available, \mathbf{C} is a 3×3 positive-semidefinite (PSD) Hermitian matrix that results in $N = 3$ eigenvalues, while, when DP SAR data are available, \mathbf{C} is still Hermitian and PSD, resulting in $N = 2$ eigenvalues. Note that, since λ is also equal to $\frac{1}{N} \text{Tr}(\mathbf{C}_{22}^{-1} \mathbf{C}_{11})$, where Tr stands for the trace, it implies that the metric we obtained is related to the well-known Wishart distance [21]–[24].

Once (4) is evaluated, the final step consists of analyzing in an objective way the discrimination capability of λ using an unsupervised approach that relies on a decision tree algorithm. The latter is designed to contrast the mean λ value, evaluated using a sliding window that scans the whole λ image, with reference mean values evaluated using regions of interest (ROIs) that fit the four mangrove areas identified by the ground truth (see Fig. 3). In detail, the λ image is partitioned into $M \times M$ tiles, and for each tile, the mean λ value is assigned to the i th mangrove class according to the following rule:

$$m_i - \frac{\epsilon_{i-1}}{2} < x \leq m_i + \frac{\epsilon_i}{2} \quad (5)$$

where x stands for the mean value evaluated within the $M \times M$ sliding window, m_i is the mean value of the i th mangrove class evaluated using the ROIs depicted in Fig. 3, and $\epsilon_0 = \epsilon_4$ is the mean value of ϵ_i ($i = 1, 2, 3$). The latter is obtained by first

sorting the mangrove classes in ascending format according to their mean λ values and, then, evaluating the difference between the mean λ values belonging to adjacent classes.

IV. EXPERIMENTS

In this section, the ability of the different polarimetric channels combinations, extracted from the C - and L -band scenes of Table I, to discriminate among mangrove species is discussed.

The first experiment is related to the C -band RadarSAT-2 scene collected in ascending pass on July 12, 2015 (see Table I). An excerpt of the VV-polarized SAR scene is shown in Fig. 3(a), where the area that includes mangrove forests is enclosed in a red box. The PMF is applied to the whole SAR scene, i.e., the test region scans the whole SAR scene, while the reference area (where evaluating C_{22}) is the area that includes the mangrove forest enclosed in the red box in Fig. 3(a). Note that the reference area that includes the mangrove forest has been selected using ground truth information and the optical data. The λ image (4) obtained processing the FP SAR scene is depicted in false color in Fig. 4. The area related to the mangroves is enclosed in the red box. By visually contrasting Fig. 4(a) with the optical image of Fig. 1, one can note that the whole mangrove forest can be easily distinguished from both the sea background and the other cultivated fields. In addition, remarkable differences among the mangrove species can be observed in the λ image. In particular, KO results in a λ signature that is well distinguishable from the other mangroves. The same analysis is undertaken on the λ image obtained processing the different DP SAR combinations [see Fig. 4(b)–(d)], which depicts the HH–VV, VV–VH, and HH–HV polarimetric channels combinations, respectively. By visually contrasting Fig. 4(b)–(d) with the optical image of Fig. 1, one can note that, once again, the whole mangrove forest can be distinguished from the surrounding environment. Even in this case, the λ signature of KO is well distinguishable from the other mangrove species. To quantitatively analyze the separability among mangrove species using λ , four ROIs (see Fig. 3) are considered that belong to areas covered by the KO, AM, AI, and AC mangroves. Note that those ROIs are manually selected using the ground truth and the optical image as reference information (see Fig. 1). The empirical probability density function (pdf) related to λ evaluated within the four ROIs is depicted in Fig. 5(a)–(d) for the FP, DP HH–VV, DP VV–VH, and DP HH–HV, respectively.

When the FP combination [see Fig. 5(a)] is considered, λ guarantees good discrimination capabilities. In particular, KO is well distinguished from the other mangroves, while AC, AM, and AI are partially overlapped, with AC and AM showing a nonnegligible level of separation. When the DP HH–VV combination is adopted [see Fig. 5(b)], KO can still be well distinguished, while AC, AM, and AI are almost completely overlapped. When the DP VV–VH combination is adopted [see Fig. 5(c)], results are similar to the HH–VV combination [see Fig. 5(b)], while the combination HH–HV provides results similar to the FP case even if KO is closer to the other mangrove types. This analysis shows that λ exhibits a good ability to discriminate among the

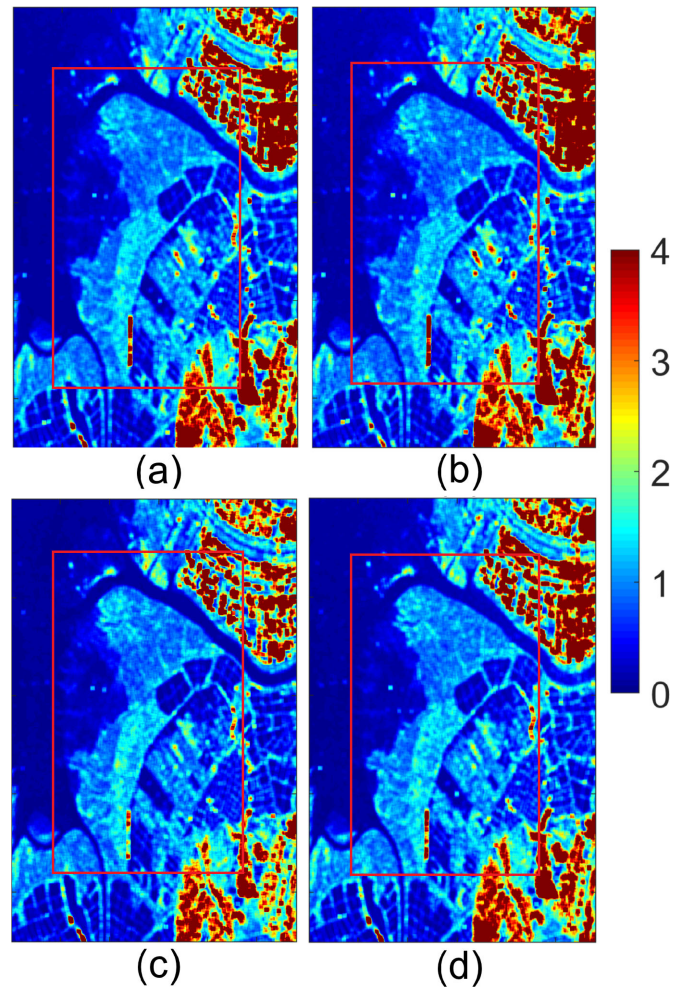


Fig. 4. False-color λ imagery obtained from the RADARSAT-2 dataset and related to different polarimetric channels combinations: (a) FP, (b) DP HH–VV, (c) DP VV–VH, and (d) DP HH–HV. The area that includes mangrove is enclosed in the red box.

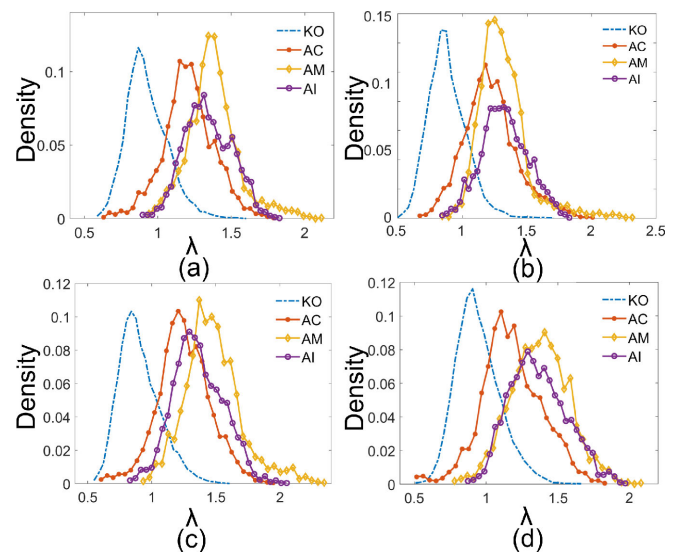


Fig. 5. Empirical pdfs evaluated over the selected ROIs using (a) FP, (b) HH–VV, (c) VV–VH, and (d) HH–HV polarimetric channels combinations.

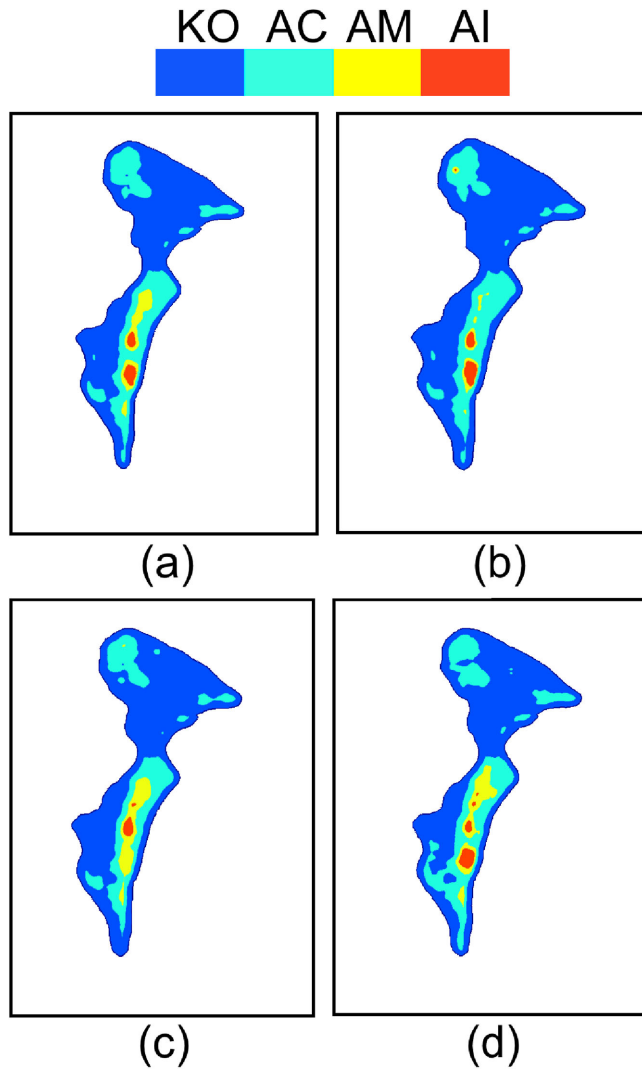


Fig. 6. Classifier outputs obtained processing λ imagery using (a) FP, (b) DP HH–VV, (c) DP VV–VH, and (d) DP HH–HV channel combinations. The classes are shown using different colors.

TABLE II
 m_i AND ϵ_i VALUES (5) EVALUATED FROM THE PDFS OF FIG. 5

	m_{KO}	m_{AC}	m_{AM}	m_{AI}	ϵ_1	ϵ_2	ϵ_3
FP	2.8264	3.6885	4.1891	4.072	0.8531	0.3873	0.1235
HH+VV	1.8091	2.4820	2.6771	2.6824	0.6729	0.1951	0.0052
HH+HV	1.9273	2.4004	2.7924	2.7605	0.4332	0.3601	0.0319
VV+VH	1.8458	2.5491	3.0029	2.7656	0.7033	0.2165	0.2373

mangrove species, and the discrimination performance varies according to the adopted polarimetric channel. The decision tree classifier is applied to the λ image obtained using the combination of FP and DP polarimetric channels in Fig. 4. The output of the classifier, which is run using an $M = 30$ sliding window, is shown in Fig. 6(a)–(d) when the FP and DP HH–HV, VV–VH, and HH–HV polarimetric combinations are used, respectively. Note that m_i and ϵ_i values [see (5)] are listed in Table II for the four mangrove classes.

By visually contrasting Fig. 6 with the optical image of Fig. 1, one can note that there is a good spatial matching between

the estimated classes and the ground truth annotated onto the optical image. In addition, the main differences between the FP and DP outputs are mainly observed within AM, AI, and AC classes. To quantitatively assess classification performance, the confusion matrix is used that consists of updating the diagonal elements when the mangrove specie is correctly estimated or the off-diagonal ones when misclassifications occur. The calculation of the confusion matrix provides descriptive parameters: the overall accuracy (OA), producer accuracy (PA), user accuracy (UA), and kappa coefficient (K) [28]. PA is the probability that a value in a given class is correctly classified; UA is the probability that a value predicted to be in a certain class really is that class; and OA measures how all the reference classes are correctly mapped. Hence, $K < 0$ ($K = 0$) stands for an accuracy that is worse (no better) than the one achieved using a random classifier, while when K tends to 1, the achieved accuracy is significantly better than the random classifier. The analysis of the confusion matrix (see Tables III and IV) shows that KO and AC can be well discriminated according to their UA scores. The other two classes exhibit a large number of misclassifications. This trend applies for all the polarimetric channel combinations, with the FP one resulting in the best performance in terms of OA and K . However, it must be pointed out that K is quite low in all the cases. This can be likely due to the ground truth information that is not enough accurate. In fact, ground surveys are not temporally collocated with the SAR acquisition, and the sampling is not dense enough to allow an accurate identification of the areas covered by different mangrove species. Hence, to provide an additional cross validation of the performance achieved by the proposed classification scheme, results are intercompared with the ones obtained using a model-based decomposition, namely the Freeman–Durden decomposition [29]. To make a fair intercomparison, a polarimetric feature associated with this decomposition is selected and processed with the decision tree classifier. In detail, the SPAN (i.e., the sum of the power associated with the elementary scattering mechanism surface, double bounce, and volumetric) extracted from the Freeman–Durden decomposition is used. Classification results are discussed using the confusion matrix in Table IV, where one can note that the performance is significantly lower than the λ one in terms of OA and K factor. It can also be noted that λ performs best independently of the polarimetric combination adopted witnessing the remarkable performance of λ in maximizing differences among the mangrove species using the polarimetric information available. An additional analysis is performed that consists of classifying the mangrove species by partitioning λ using the Wishart classifier [21] instead of the decision tree. This analysis, which stems from the fact that λ is intrinsically related to the Wishart distance, consists of evaluating λ over four polygons associated with the four mangrove types. After that, the classification is undertaken following the Wishart classification approach [21], i.e., by using the minimum distance criterion. Results obtained using the different polarimetric combinations are listed in Table IV. It can be noted that the Wishart classifier results in a classification accuracy that is significantly lower than the one obtained by processing λ with the decision tree algorithm.

TABLE III
CONFUSION MATRIX RELATED TO THE FIRST EXPERIMENT

		Predicted class																	
		FP					HH+VV					HH+HV					VV+VH		
True class	KO	AC	AM	AI	KO	AC	AM	AI	KO	AC	AM	AI	KO	AC	AM	AI			
	AC	36981	7226	331	94	37729	6673	108	122	34604	9172	715	87	37361	6653	500	118		
	AM	1541	4079	0	0	1470	4027	110	13	1659	3961	0	0	1749	3855	16	0		
	AI	143	2033	1445	200	227	3011	402	181	122	1650	1850	199	125	1858	1525	313		
	AI	238	2604	927	640	203	2851	544	811	173	2414	1071	751	254	2310	1756	89		

TABLE IV
UA, PA, OA, AND K RELATED TO THE FIRST EXPERIMENT

Feature	UA (%)				PA (%)				OA (%)	K (%)
	KO	AC	AM	AI	KO	AC	AM	AI		
FP	82.9	72.6	37.8	14.5	95.1	25.6	53.5	68.5	73.77	43.22
HH+VV	84.5	71.7	10.5	18.4	95.2	24.3	34.5	72	73.47	41.43
HH+HV	77.6	70.5	48.4	17	94.7	23	50.9	72.4	70.46	39.57
VV+VH	83.7	68.6	39.9	2	94.6	26.3	40.2	17.1	73.24	41.26
FD decomposition	54.55	9	87.68	48.55	95.2	28.1	18.23	40.7	52	27.52
Wishart FP	78.92	21.14	27.61	39.01	87.5	18.82	31.8	20	67	26.6
Wishart HH+VV	68.1	33.7	24.9	46.3	92	16.3	20.3	22.3	60.3	25.54
Wishart HH+HV	61.3	33.5	46.5	35.1	90.3	14.9	20.5	22.4	55.7	21.65
Wishart VV+VH	68.3	39.6	40.6	28.8	91.5	19.7	26.5	15.8	60.8	25.9

TABLE V
CONFUSION MATRIX RELATED TO THE SECOND EXPERIMENT

		Predicted class																	
		FP					HH+VV					HH+HV					VV+VH		
True class	KO	AC	AM	AI	KO	AC	AM	AI	KO	AC	AM	AI	KO	AC	AM	AI			
	AC	51972	20232	2972	20846	44464	24195	5104	24537	51730	22173	2708	21081	46254	27028	3344	20995		
	AM	85	13447	0	0	1134	12417	0	0	87	13464	0	0	342	13206	0	0		
	AI	231	53	7647	5288	388	67	7757	5007	343	66	7780	5030	138	5	8013	5063		
	AI	1849	9	846	8221	3456	9	1158	6302	2050	9	1004	7862	395	3	1049	9478		

TABLE VI
UA, PA, OA, AND K RELATED TO THE SECOND EXPERIMENT

Feature	UA (%)				PA (%)				OA (%)	K (%)
	KO	AC	AM	AI	KO	AC	AM	AI		
FP	54.1	99.4	57.8	75.2	96	39.9	66.7	23.9	60.80	40.07
HH+VV	45.2	91.6	58.7	57.7	89.9	33.8	55.3	17.6	52.16	29.56
HH+HV	53	99.4	58.9	72	95.4	37.7	67.7	23.1	59.71	38.59
VV+VH	47.4	97.5	60.6	86.8	98.1	32.8	64.6	26.7	56.87	37.38
FD decomposition	48.17	73.01	40.35	40.51	82.19	34.76	36.36	14.73	48.97	21.94
Wishart FP	67.9	53.3	38.2	33.6	81.6	36.1	38.2	17.1	61	25.3
Wishart HH+VV	39	75.6	49.4	42.5	87.8	25.3	28.1	15.3	43.8	20
Wishart HH+HV	39.5	87	54.2	33.4	84.6	28.1	29.4	14.2	45	20.5
Wishart VV+VH	36.8	83.5	52.9	40.3	85	25.6	30.8	15.5	43.2	19.6

The second experiment is related to the L -band ALOS-2 scene (see Table I). An excerpt of the VV-polarized image is shown in Fig. 3(b), where the area that includes mangrove forests is enclosed in a red box. Even in this case, PMF processing is applied to the FP SAR scene, and the reference area that covers the whole mangrove forests is selected using the optical data as reference information. The λ output related to the different channel combinations is shown in Fig. 7. Even in this case, by visually contrasting Fig. 7 with the optical image of Fig. 1, one can note that distinguishable features can be associated with different mangrove species. However, the visual discrimination results to be more difficult in this case. From a physical viewpoint, it must be noted that the larger wavelength at the L -band makes ground scattering a more dominant contribution. To further discuss the discrimination capability of the λ feature, empirical pdfs related to the four classes are sketched in Fig. 8 using four ROIs visually inspected using the ground truth information. Unlike the C -band imagery, in this case, the largest separation is provided by the AC

class that is well separated by all the other mangrove species for all the polarimetric combinations. The remaining three classes are partially overlapped. This overlapping is very pronounced when dealing with the DP HH-VV and HH-HV combinations [see Fig. 8(b) and (d)]. To discuss separation capability in an objective way, the decision tree classifier is used, whose output is shown in Fig. 9(a)-(d) for the FP, DP HH-VV, DP VV-VH, and DP HH-HV cases, respectively. By visually contrasting the classifier output with the ground truth annotated in Fig. 1, one can note a good visual matching of the different classes. Note that there are remarkable differences among the classifier outputs related to the C - and L -band cases that are likely due to the different wavelength and the different acquisition days that fall into different seasons. Even in this case, to quantitatively judge the classification performance, the confusion matrix is used (see Tables V and VI). The latter confirms that the best performance, in terms of OA, is provided by the FP combination. In addition, the AC species results in the best discrimination with the other

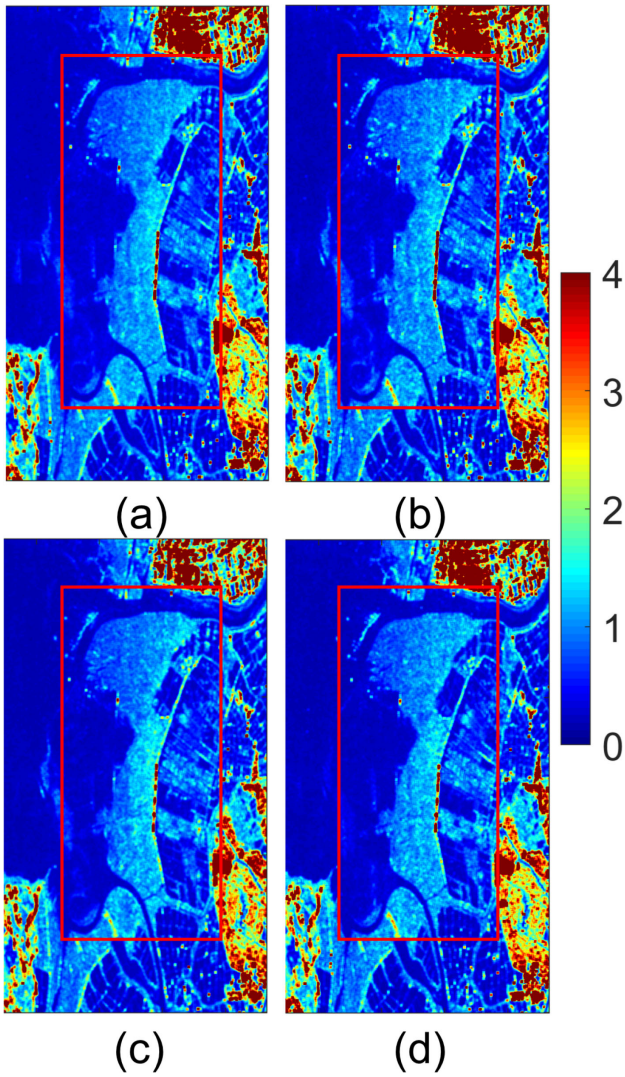


Fig. 7. False color λ imagery obtained from the ALOS-2 dataset and related to different polarimetric channels combinations: (a) FP, (b) DP HH-VV, (c) DP VV-VH, and (d) DP HH-HV. The area that includes mangrove is enclosed in the red box.

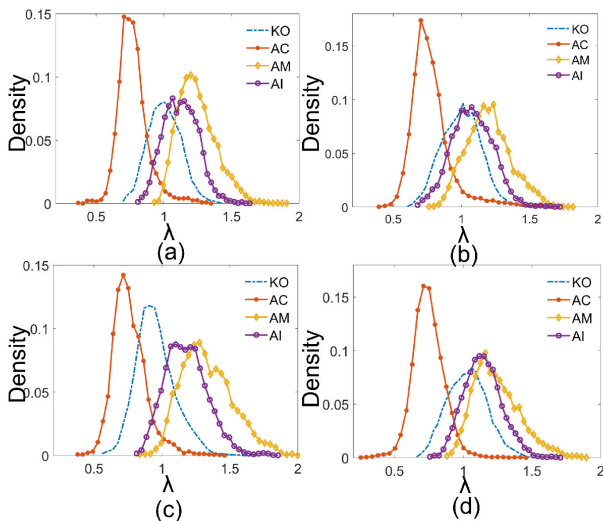


Fig. 8. Empirical pdfs evaluated over the selected ROIs using (a) FP, (b) HH-VV, (c) VV-VH, and (d) HH-HV polarimetric channel combinations.

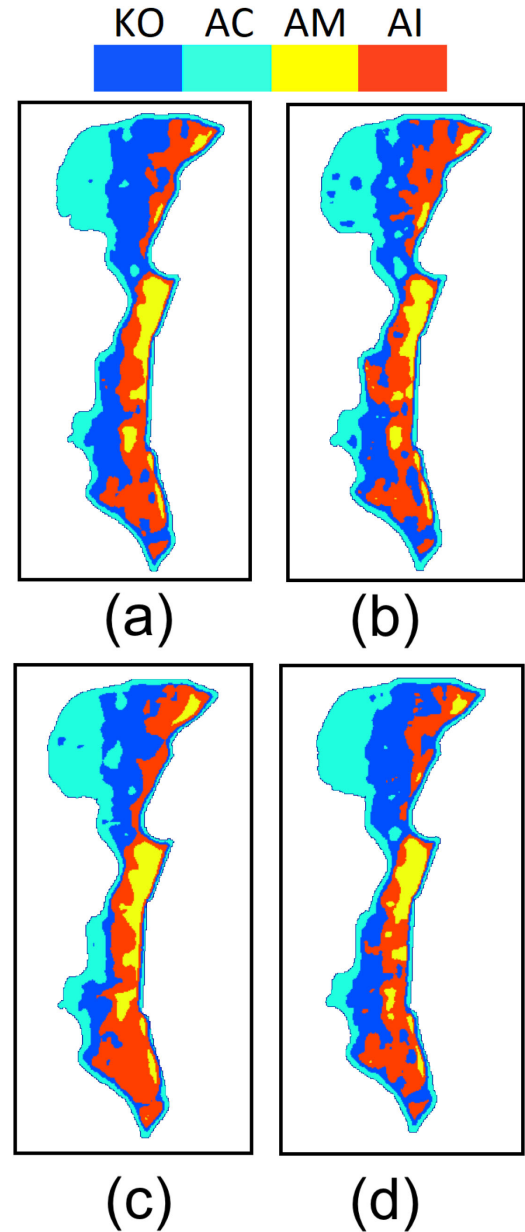


Fig. 9. Classifier outputs obtained processing λ imagery using (a) FP, (b) DP HH-VV, (c) DP VV-VH, and (d) DP HH-HV channel combinations. The classes are shown using different colors.

three classes providing remarkable performance in terms of UA. The classification performance is contrasted with the one achieved using the model-based feature (see Table VI). Even in this case, λ performs best. In addition, the classification accuracy obtained using the Wishart classifier instead of the decision tree algorithm is listed in Table VI for all the polarimetric combinations. It can be noted that, again, the Wishart classifier performs worse than the joint use of λ and the decision tree algorithm.

V. CONCLUSION

A polarimetric change detector approach is used to analyze the sensitivity of PolSAR measurements to different mangrove

species. The change detector scheme results in a feature (λ), which is applied to the L - and C -band PolSAR scheme to test its discrimination capabilities. Experiments, undertaken on actual PolSAR data collected on the MPMNR, Hong Kong, show the following.

- 1) The λ feature, which is intrinsically connected to the Wishart distance, provides good discrimination performance, being able to discriminate, in both C - and L -band cases, two out of the four mangrove identified by the ground truth.
- 2) The λ feature outperforms conventional model-based features in terms of discrimination performance.
- 3) The decision tree classifier outperforms the conventional Wishart distance approach at both L - and C -bands.
- 4) C - and L -band PolSAR data provide complementary discrimination results that suggest a joint use of multifrequency PolSAR measurements to improve discrimination performance.

REFERENCES

- [1] M. Wilkie and S. Fortuna, *Status and Trends in Mangrove Area Extent Worldwide*. Rome, Italy: Forestry Department, Food and Agriculture Organization of the United Nations, 2003.
- [2] C. Giri, "Observation and monitoring of mangrove forests using remote sensing: Opportunities and challenges," *Remote Sens.*, vol. 8, no. 9, 2016, Art. no. 783.
- [3] C. Kuenzer, A. Bluemel, S. Gebhardt, T. V. Quoc, and S. Dech, "Remote sensing of mangrove ecosystems: A review," *Remote Sens.*, vol. 3, no. 5, pp. 878–928, 2011.
- [4] L. Wang, M. Jia, D. Yin, and J. Tian, "A review of remote sensing for mangrove forests: 1956–2018," *Remote Sens. Environ.*, vol. 231, 2019, Art. no. 111223.
- [5] C. Giri *et al.*, "Status and distribution of mangrove forests of the world using earth observation satellite data," *Global Ecol. Biogeogr.*, vol. 20, no. 1, pp. 154–159, 2011.
- [6] K. W. Krauss and D. A. Friess, "World atlas of mangroves," *Wetlands*, vol. 31, no. 5, Sep. 2011, Art. no. 1003.
- [7] N. Thomas, R. Lucas, P. Bunting, A. Hardy, A. Rosenqvist, and M. Simard, "Distribution and drivers of global mangrove forest change, 1996–2010," *PLOS ONE*, vol. 12, no. 6, pp. 1–14, 2017.
- [8] M. Kamal, S. Phinn, and K. Johansen, "Object-based approach for multi-scale mangrove composition mapping using multi-resolution image datasets," *Remote Sens.*, vol. 7, no. 4, pp. 4753–4783, 2015.
- [9] Y. Zhu, K. Liu, L. Liu, S. Wang, and H. Liu, "Retrieval of mangrove aboveground biomass at the individual species level with worldview-2 images," *Remote Sens.*, vol. 7, no. 9, pp. 12192–12214, 2015.
- [10] L. Wang, W. P. Sousa, and P. Gong, "Integration of object-based and pixel-based classification for mapping mangroves with IKONOS imagery," *Int. J. Remote Sens.*, vol. 25, no. 24, pp. 5655–5668, 2004.
- [11] L. Wang, W. P. Sousa, P. Gong, and G. S. Biging, "Comparison of IKONOS and QuickBird images for mapping mangrove species on the Caribbean coast of Panama," *Remote Sens. Environ.*, vol. 91, no. 3, pp. 432–440, 2004.
- [12] M. Migliaccio, L. Mascolo, F. Nunziata, M. Sarti, and G. Mazzarella, "COSMO-SkyMed HH/VV pingpong mode SAR data to discriminate among sea, urban, and vegetated areas," *IEEE J. Sel. Topics Appl. Earth Observ. Remote Sens.*, vol. 7, no. 7, pp. 2880–2894, Jul. 2014.
- [13] H. Zhang *et al.*, "Potential of combining optical and dual polarimetric SAR data for improving mangrove species discrimination using rotation forest," *Remote Sens.*, vol. 10, no. 3, 2018, Art. no. 467.
- [14] F. R. de Souza Pereira, M. Kampel, and M. Cunha-Lignon, "Mapping of mangrove forests on the southern coast of São Paulo, Brazil, using synthetic aperture radar data from ALOS/PALSAR," *Remote Sens. Lett.*, vol. 3, no. 7, pp. 567–576, 2012.
- [15] B. Chen *et al.*, "A mangrove forest map of China in 2015: Analysis of time series Landsat 7/8 and Sentinel-1A imagery in Google Earth Engine cloud computing platform," *ISPRS J. Photogramm. Remote Sens.*, vol. 131, pp. 104–120, 2017.
- [16] A. Aslan, A. F. Rahman, M. W. Warren, and S. M. Robeson, "Mapping spatial distribution and biomass of coastal wetland vegetation in Indonesian Papua by combining active and passive remotely sensed data," *Remote Sens. Environ.*, vol. 183, pp. 65–81, 2016.
- [17] T. D. Pham, D. T. Bui, K. Yoshino, and N. N. Le, "Optimized rule-based logistic model tree algorithm for mapping mangrove species using ALOS PALSAR imagery and GIS in the tropical region," *Environ. Earth Sci.*, vol. 77, no. 5, Feb. 2018, Art. no. 159.
- [18] I. Brown, S. Mwansasu, and L.-O. Westerberg, "L-band polarimetric target decomposition of mangroves of the Rufiji Delta, Tanzania," *Remote Sens.*, vol. 8, no. 2, 2016, Art. no. 140.
- [19] L. M. Novak, M. B. Sechtin, and M. J. Cardullo, "Studies of target detection algorithms that use polarimetric radar data," *IEEE Trans. Aerosp. Electron. Syst.*, vol. 25, no. 2, pp. 150–165, Mar. 1989.
- [20] A. Marino and I. Hajnsek, "A change detector based on an optimization with polarimetric SAR imagery," *IEEE Trans. Geosci. Remote Sens.*, vol. 52, no. 8, pp. 4781–4798, Aug. 2014.
- [21] J.-S. Lee, M. R. Grunes, T. L. Ainsworth, L.-J. Du, D. L. Schuler, and S. R. Cloude, "Unsupervised classification using polarimetric decomposition and the complex Wishart classifier," *IEEE Trans. Geosci. Remote Sens.*, vol. 37, no. 5, pp. 2249–2258, Sep. 1999.
- [22] V. Akbari, S. N. Anfinsen, A. P. Doulgeris, T. Eltoft, G. Moser, and S. B. Serpico, "Polarimetric SAR change detection with the complex Hotelling–Lawley trace statistic," *IEEE Trans. Geosci. Remote Sens.*, vol. 54, no. 7, pp. 3953–3966, Jul. 2016.
- [23] M. Sarti, M. Migliaccio, F. Nunziata, L. Mascolo, and E. Brugnoli, "On the sensitivity of polarimetric SAR measurements to vegetation cover: The Coiba National Park, Panama," *Int. J. Remote Sens.*, vol. 38, no. 23, pp. 6755–6768, 2017.
- [24] A. Buono, F. Nunziata, M. Migliaccio, X. Yang, and X. Li, "Classification of the yellow river delta area using fully polarimetric SAR measurements," *Int. J. Remote Sens.*, vol. 38, no. 23, pp. 6714–6734, 2017.
- [25] S. Cloude, *Polarisation: Applications in Remote Sensing*. Oxford, U.K.: Oxford Univ. Press, 2009.
- [26] J. Lee and E. Pottier, *Polarimetric Radar Imaging: From Basics to Applications*. Boca Raton, FL, USA: CRC Press, 2009.
- [27] A. Marino and A. Alonso-Gonzalez, "An optimization of the difference of covariance matrices for PolSAR change detection," in *Proc. IEEE Int. Geosci. Remote Sens. Symp.*, Jul. 2017, pp. 5315–5318.
- [28] J. R. Jensen, *Introductory Digital Image Processing: A Remote Sensing Perspective*, 4th ed. Englewood Cliffs, NJ, USA: Prentice-Hall, 2015.
- [29] A. Freeman and S. L. Durden, "A three-component scattering model for polarimetric SAR data," *IEEE Trans. Geosci. Remote Sens.*, vol. 36, no. 3, pp. 963–973, May 1998.



Emanuele Ferrentino (Student Member, IEEE) was born in Cattolica, Italy, in 1984. He received the Ph.D. degree in information engineering from the Università degli Studi di Napoli "Parthenope," Napoli, Italy, in 2019.

He is currently a Postdoctoral Researcher with the Università degli Studi di Napoli "Parthenope." His research interests include electromagnetic modeling, polarimetric synthetic aperture radar data analysis, and remote sensing land and marine applications (earthquake damage assessment, target detection, coastline extraction, and classification).



Ferdinando Nunziata (Senior Member, IEEE) was born in Avellino, Italy, in 1982. He received the Ph.D. degree in telecommunication engineering from the Università degli Studi di Napoli "Parthenope," Napoli, Italy, in 2008.

Since 2019, he has been Associate Professor with the Università degli Studi di Napoli "Parthenope." His current research interests include remote sensing for marine and coastal applications, polarimetry, inverse problems for microwave remote sensing applications, and reverberating chambers.

Dr. Nunziata has been an Associate Editor for the IEEE JOURNAL OF SELECTED TOPICS IN APPLIED EARTH OBSERVATIONS AND REMOTE SENSING (JSTARS) since 2019.



Hongsheng Zhang (Member, IEEE) received the B.Eng. degree in computer science and technology and the M.Eng. degree in computer applications technology from South China Normal University, Guangzhou, China, in 2007 and 2010, respectively, and the Ph.D. degree in earth system and geoinformation science from the Chinese University of Hong Kong, Sha Tin, Hong Kong, in 2013.

He is currently an Assistant Professor with the Department of Geography, The University of Hong Kong, Pok Fu Lam, Hong Kong. His research interests include remote sensing applications in tropical and subtropical areas, with a focus on urban environment, mangroves and natural disasters monitoring, using multisource remote sensing data fusion and image pattern recognition techniques.



Maurizio Migliaccio (Fellow, IEEE) was born in Napoli, Italy, in 1962. He received the Laurea degree (hons.) in electronic engineering from the Università degli Studi di Napoli “Federico II”, Napoli, Italy, in 1987.

He is a Full Professor of Electromagnetics with the Università degli Studi di Napoli “Parthenope”, Napoli, Italy. His current scientific interests include remote sensing for marine and coastal applications, polarimetry, problems for microwave remote sensing applications, and reverberating chambers.